

Solar EUV and XUV energy input to thermosphere on solar rotation time scales derived from photoelectron observations

W. K. Peterson,¹ T. N. Woods,¹ J. M. Fontenla,¹ P. G. Richards,² P. C. Chamberlin,³ S. C. Solomon,⁴ W. K. Tobiska,⁵ and H. P. Warren⁶

Received 17 November 2011; revised 27 February 2012; accepted 5 April 2012; published 18 May 2012.

[1] Solar radiation below ~ 100 nm produces photoelectrons, a substantial portion of the F region ionization, most of the E region ionization, and drives chemical reactions in the thermosphere. Unquantified uncertainties in thermospheric models exist because of uncertainties in solar irradiance models used to fill spectral and temporal gaps in solar irradiance observations. We investigate uncertainties in solar energy input to the thermosphere on solar rotation time scales using photoelectron observations from the FAST satellite. We compare observed and modeled photoelectron energy spectra using two photoelectron production codes driven by five different solar irradiance models. We observe about 1.7% of the ionizing solar irradiance power in the escaping photoelectron flux. Most of the code/model pairs used reproduce the average escaping photoelectron flux over a 109-day interval in late 2006. The code/model pairs we used do not completely reproduce the observed spectral and solar rotation variations in photoelectron power density. For the interval examined, 30% of the variability in photoelectron power density with equivalent wavelengths between 18 and 45 nm was not captured in the code/model pairs. For equivalent wavelengths below ~ 16 nm, most of the variability was missed. This result implies that thermospheric model runs based on the solar irradiance models we tested systematically underestimate the energy input from ionizing radiation on solar rotation time scales.

Citation: Peterson, W. K., T. N. Woods, J. M. Fontenla, P. G. Richards, P. C. Chamberlin, S. C. Solomon, W. K. Tobiska, and H. P. Warren (2012), Solar EUV and XUV energy input to thermosphere on solar rotation time scales derived from photoelectron observations, *J. Geophys. Res.*, *117*, A05320, doi:10.1029/2011JA017382.

1. Introduction

[2] The Earth's thermosphere is heated primarily by solar radiation. Extensive model runs of large-scale, community-based, thermospheric general circulation models are now the best way to interpret how changes in energy inputs from solar irradiance, Joule heating, and particle precipitation are distributed to the thermosphere during periods of solar and geomagnetic activity. However, the quantitative limitations,

and therefore usefulness of these models, on solar rotation time scales remains to be determined. Here we present photoelectron observations for 109 days in late 2006, near the end of solar cycle 23. We use solar irradiance models and photoelectron production codes to evaluate the uncertainty in energy input to the thermosphere associated with uncertainties in photochemical models and in the spectral and temporal variability of solar irradiance on solar rotation time scales.

[3] There has been continual improvement in both the spectral and temporal resolution of solar irradiance observations over the years, but only since the launch of NASA's Solar Dynamics Observatory (SDO) have the high temporal, high spectral resolution observations of solar irradiance at wavelengths between ~ 1 and ~ 100 nm necessary for aeronomic calculations become available [Woods *et al.*, 2010]. To fill the historical spectral and temporal gaps in our knowledge of solar EUV and XUV observations, empirical, first principles, and observation driven solar irradiance models have been developed. These models are needed especially for the ionizing wavelengths below ~ 45 nm where solar EUV and XUV radiation is most variable. As shown below, the spectral character of solar irradiance models differ significantly from each other and available observations.

¹Laboratory for Atmospheric and Space Physics, University of Colorado at Boulder, Boulder, Colorado, USA.

²Physics Department, George Mason University, Fairfax, Virginia, USA.

³NASA Goddard Space Flight Center, Greenbelt, Maryland, USA.

⁴High Altitude Observatory, National Center for Atmospheric Research, Boulder, Colorado, USA.

⁵Space Weather Center, Utah State University, Logan, Utah, USA.

⁶Space Science Division, Naval Research Laboratory, Washington, DC, USA.

Corresponding author: W. K. Peterson, Laboratory for Atmospheric and Space Physics, University of Colorado at Boulder, Boulder, CO 80303, USA. (bill.peterson@lasp.colorado.edu)

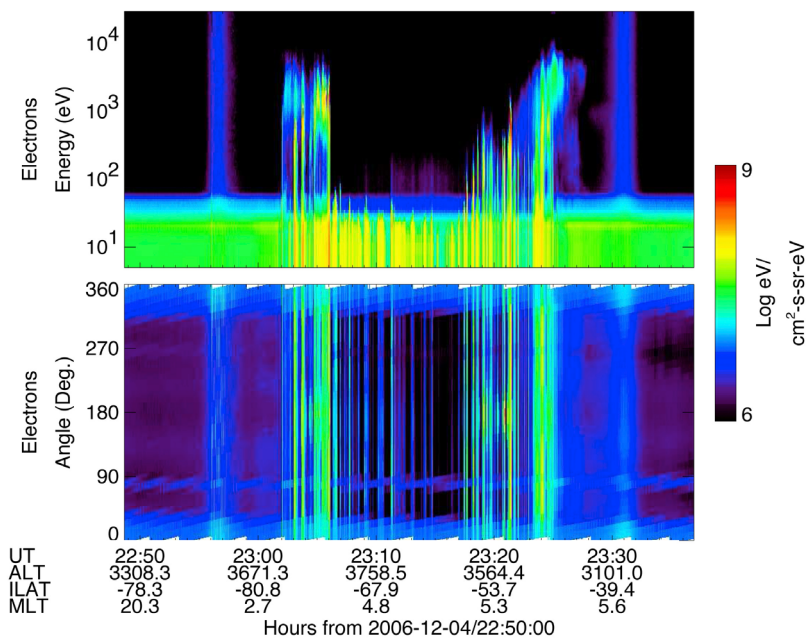


Figure 1. Energetic electron spectra observed on December 4, 2006. (top) Angle averaged electron energy spectra from 3 eV to 33 keV as a function of time encoded in units of $\log_{10} (\text{cm}^2\text{-s-sr-eV})^{-1}$ by the color bar on the right. (bottom) The 100 eV to 33 keV energy averaged angle time spectra as a function of time encoded in the same units. The time (UT) of data acquisition and altitude in kilometers (ALT), invariant latitude in degrees (ILAT) and magnetic local time in decimal hours (MLT) of the FAST satellite are shown at the bottom.

[4] Photoelectrons are efficiently and immediately produced. They have been used as an indicator of the varying intensity of solar ionizing radiation for many years [e.g., *Dalgarno et al.*, 1973]. This study relies on the photoelectron observations from the Fast Auroral Snapshot (FAST) satellite [*Carlson et al.*, 2001] to provide the measurements to which model calculations are compared. Previous comparisons have been made between FAST photoelectron observations and calculated photoelectron energy spectra during two solar flares [*Woods et al.*, 2003; *Peterson et al.*, 2008] and for three days with minimal solar activity in 2002, 2003, and 2008 [*Peterson et al.*, 2009]. *Peterson et al.* [2008] demonstrated that, on solar flare time scales, the uncertainties in photoelectron observations and the Flare Irradiance Spectral Model (FISM) [*Chamberlin et al.*, 2007, 2008] were comparable for ionizing radiation below 45 nm. *Peterson et al.* [2009] found the largest differences between observed and modeled fluxes are in the 4–10 nm range, where photoelectron data from the FAST satellite indicate that the Thermosphere, Ionosphere, Mesosphere, Energetics, and Dynamics (TIMED) / Solar Extreme Ultraviolet Experiment (SEE) Version 9 irradiances are systematically low. Their analysis also suggested that variation on solar cycle timescales in the TIMED/SEE Version 9 data and the FISM irradiance derived from them are systematically low in the 18–27 nm range. This paper examines variability on solar rotation time scales using daily average photoelectron fluxes acquired from FAST during the period of September 14th to December 31st, 2006 and compares them to photoelectron fluxes calculated from combinations of two photoelectron production codes and five solar irradiance models.

[5] Photoelectron observations were made from the FAST satellite from 1997 to 2008. We use data acquired at altitudes above 1500 km equatorward of the auroral oval. The paper is organized as follows. We briefly discuss the technique, solar irradiance observations, irradiance models, and photoelectron production codes. We present daily averaged observed photoelectron fluxes and those calculated from the suite of code/irradiance model pairs for the last 109 days in 2006. The calculated and observed photoelectron data are compared in multiple formats to explore the spatial and spectral variability of the photoelectron power density on solar rotation time scales as well as over the entire interval. Finally, the implications of the comparisons on the reliability of solar irradiance models in the 2–45 nm range on solar rotation time scales are discussed.

2. Photoelectron Observations

[6] Figure 1 presents observations of energetic electrons observed on the FAST spacecraft during one apogee over the southern pole on December 4, 2006. The electron energy spectra displayed in spectrogram format are from the Electron Electrostatic Analyzers (EESA) detectors [*Carlson et al.*, 2001]. Only data obtained when the FAST satellite was equatorward of the region of auroral zone electrons (e.g., before $\sim 23:05$ and after $\sim 23:25$ in Figure 1) were used in this investigation. The narrow band of emissions at about 25 eV seen equatorward of the auroral ovals in the top energy-time spectrogram is the signature of electrons produced by photoionization of N_2 and O in the ionosphere below the spacecraft by the intense 30.4 nm HeII solar emission line [*Doering et al.*, 1976]. The FAST electron

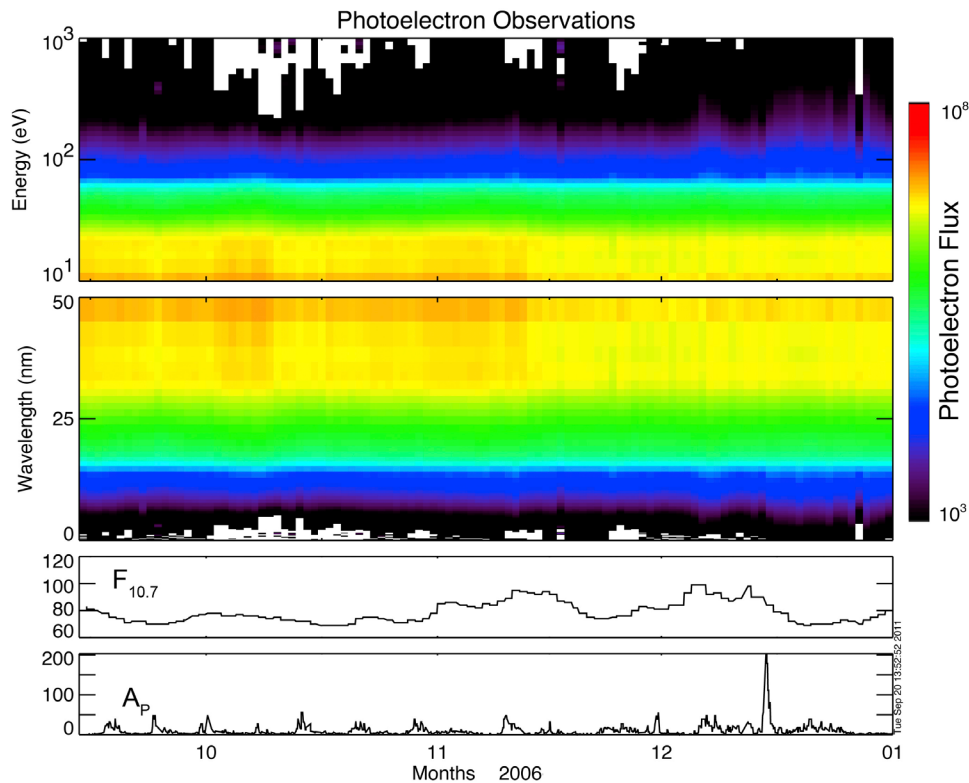


Figure 2. Observed daily averaged photoelectron energy spectra from September 14 through December 31, 2006. Data are presented in the top two panels in energy-time spectrogram format. The logarithm of the photoelectron fluxes is encoded in units of $(\text{cm}^2\text{-s-sr-keV})^{-1}$ by the color bar on the right. The top panel displays the flux as a function of energy in units of electron volts. The second panel displays the same flux as a function of equivalent wavelength in nm (see text). Also shown are the solar $F_{10.7}$ and planetary magnetic A_P indices.

spectrometer has a 360° field of view that includes the magnetic field direction. The instrument samples all pitch angles simultaneously. The energy-averaged pitch angle spectra in Figure 1 (bottom) show several horizontal bands. Electron pitch angles in the range 0 – 180° are related to the angle shown as follows: From 0 to 180° pitch angle equals the angle shown; from 180 to 360° pitch angle equals 360 minus the angle shown. The widest and most intense band is near angles of 0 or 360 degrees, which corresponds to energetic photoelectrons coming up field lines from their source in the southern hemisphere ionosphere. The width of the band of upflowing photoelectrons is determined by the relative strengths of the magnetic field at the satellite and at the top of the ionosphere. The two narrower horizontal bands near angles of 90° and 270° are produced by photoelectrons generated on spacecraft surfaces that are directed to the electron detectors as they circle the local magnetic field after they are produced. The weak horizontal band appearing near 180° corresponds to down flowing electrons in the southern hemisphere. These bands are the backscattered photoelectrons that are generated in the dark magnetically conjugate northern hemisphere from the photoelectrons that are observed streaming up from the sunlit southern hemisphere [Richards and Peterson, 2008]. Penetrating radiation in the ring current introduces a background signal independent of energy and angle as seen at $\sim 22:57$ and $\sim 23:30$ in Figure 1.

[7] The observed photoelectron spectra are processed to remove noise from penetrating radiation and to improve the signal-to-noise ratio. To increase the signal to noise at higher energies, we use one-minute averages of the data limited to pitch angles corresponding to ionospheric photoelectrons. This removes all spacecraft generated photoelectrons from our analysis. We remove the background signal generated by penetrating radiation as described in Woods *et al.* [2003]. A correction for the spacecraft potential is made by finding the best fit between the processed spectra and model photoelectron spectra in the region near 60 eV. This region in the spectrum corresponds to a sharp drop in solar irradiance below ~ 16 nm. To increase the signal-to-noise ratio further, we consider only daily average photoelectron spectra. Because FAST data are not continuously acquired, the number of usable one-minute spectra per day is determined by orbital position and spacecraft operations. For a more complete description of the processing, see Peterson *et al.* [2009].

[8] Figure 2 shows spectrograms of processed daily averaged observed photoelectron energy spectra for the interval at the end of 2006 under investigation. To facilitate comparisons between photoelectron energy spectra and solar irradiance data, the photoelectron energy spectra are presented as a function of equivalent wavelength in the second panel of Figure 2. Equivalent wavelength is calculated assuming a constant 15 eV ionization potential. This interval

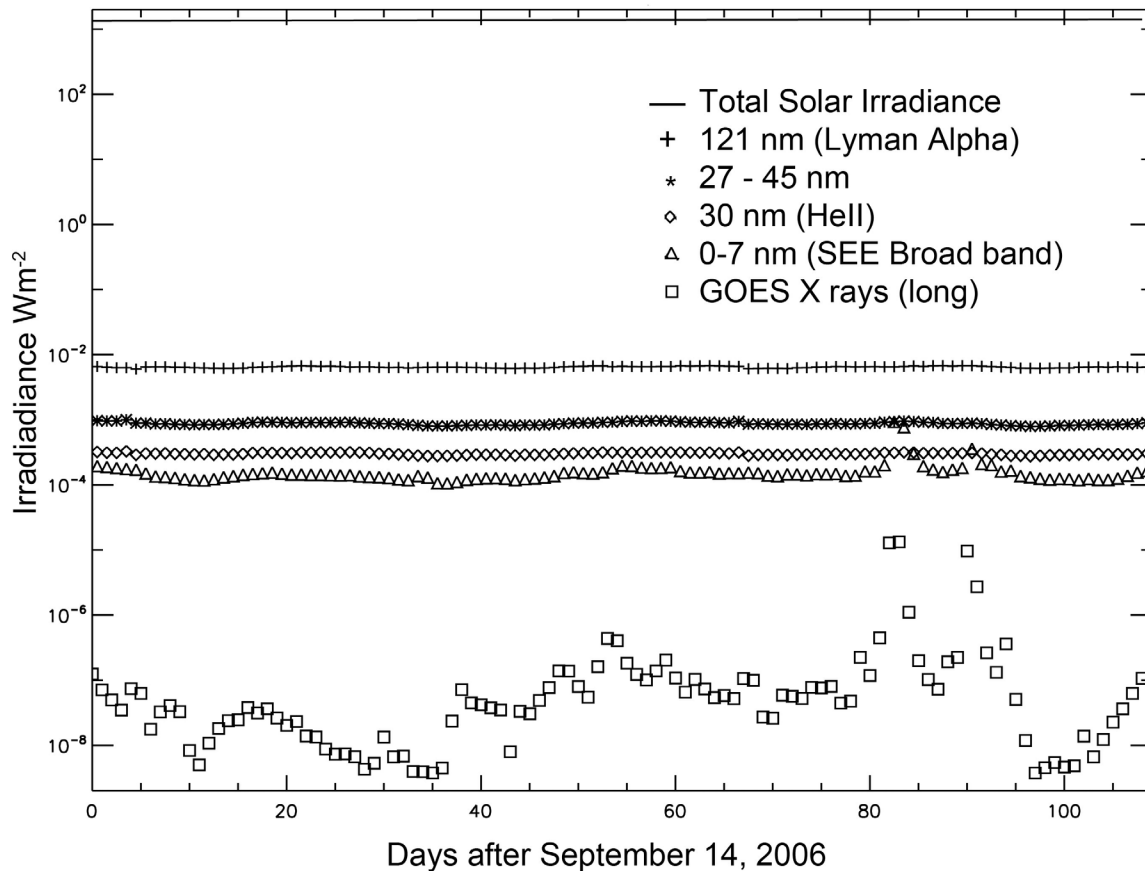


Figure 3. Daily average values of observed total and partial solar irradiance for the interval from September 14 to December 31, 2006 from the SORCE, TIMED, and GOES satellites in units of W/m^2 . See text.

has modest solar activity as indicated by the $F_{10.7}$ index and four X class flares in December. Because of the precession of the FAST orbit, data are primarily from the northern hemisphere before November 7 and from the southern hemisphere after. Also after November 7 most of the data were acquired near the terminator where the solar zenith angle was near to but less than 90° . This interval was also noteworthy for the recurring low-level geomagnetic activity driven by variations in the solar wind speed as seen in the A_p index and discussed by *Thayer et al.* [2008] and others. Variations of the photoelectron energy spectra over solar rotational periods are not prominent in the logarithmic intensity scale used in Figure 2. They are readily apparent however in the differential analysis presented below.

3. Solar Irradiance Observations and Models

[9] Only a very small fraction of solar irradiance produces photoelectrons. Figure 3 presents line plots of total and representative band restricted solar irradiance observations during the interval shown in Figure 2. Total solar irradiance incident on Earth observed on the SORCE satellite varied from $1345.1423 \pm 0.5169 \text{ W/m}^2$ on September 14 to $1407.6471 \pm 0.4961 \text{ W/m}^2$ on December 31, 2006 as the Earth-Sun distance decreased [*Kopp and Lean, 2011*]. The band restricted data presented in Figure 3 and the rest of the

paper have been adjusted to constant 1 astronomical unit (AU) values. During this interval, 1 nm resolution irradiance measurements above 27 nm were available from the Solar EUV Experiment (SEE) instrument on the Thermosphere Ionosphere Mesosphere Energetics and Dynamics (TIMED) Satellite [*Woods et al., 1998*]. Below 27 nm, broadband irradiance observations are available from TIMED/SEE and an instrument on the NOAA/GOES series of satellites [*Garcia, 1994*]. Shown in Figure 3 are 1 nm resolution irradiances including the Lyman alpha (121.6 nm) and HeII (30.4 nm) lines as well as data from the 0.1–7 nm TIMED/SEE and 0.1–0.8 nm GOES sensors. Also presented in Figure 3 are the integrated irradiance from 27 to 45 nm obtained from TIMED/SEE observations. There is no complete spectral coverage of the region below 27 nm for the time interval of interest. Systematic high-resolution (0.1–1 nm) solar irradiance data from 6 to 27 nm only became available with the launch of the EUV Variability Experiment (EVE) on the Solar Dynamics Observatory (SDO) in February 2010 [*Woods et al., 2010*].

[10] Photoelectrons are directly produced by EUV radiation at wavelengths less than ~ 100 nm. However, photoelectrons with equivalent wavelengths shorter than ~ 35 nm are overwhelmed by secondary photoelectrons produced by higher energy photoelectrons. About half of the ionizing radiation power occurs below 27 nm where measurements,

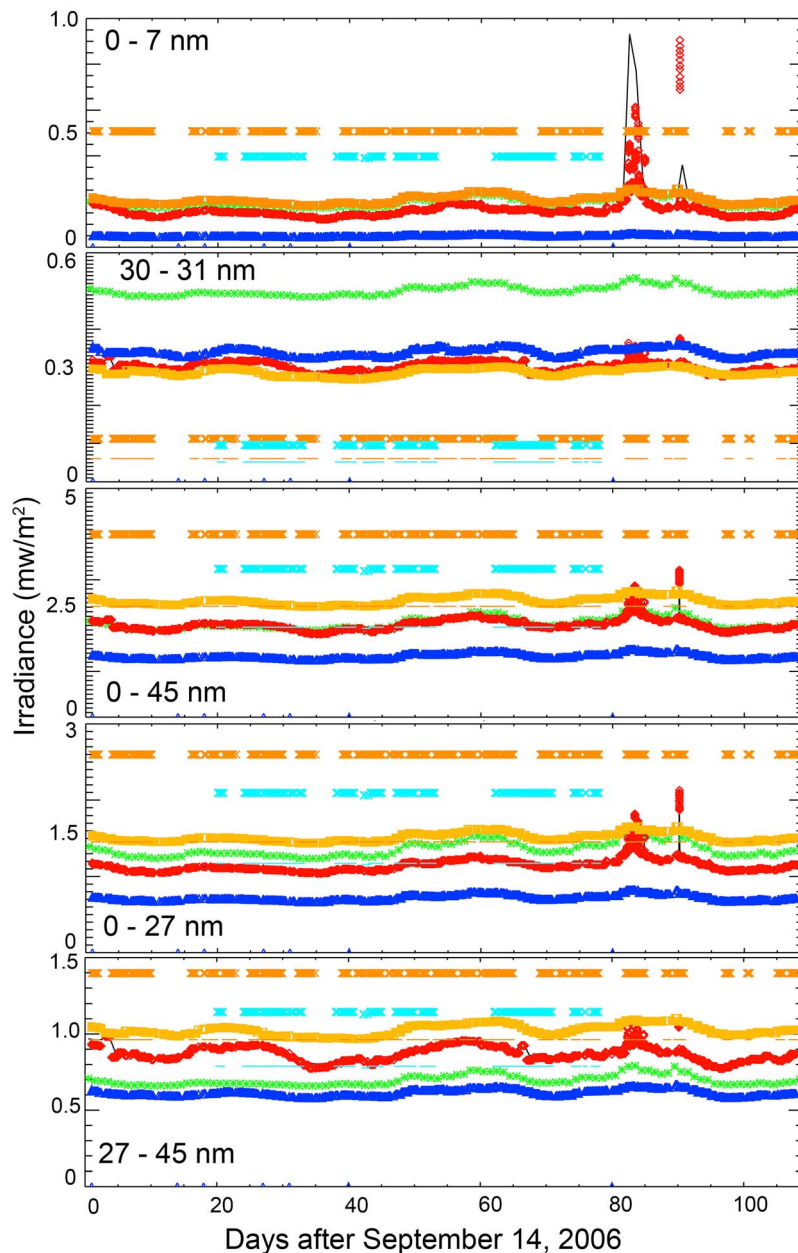


Figure 4. Predicted and observed solar irradiance in the indicated wavelength regions as a function time for the interval in late 2006. Irradiance values are presented in units of mW/m^2 . Note that different irradiance ranges are used for each wavelength band, which is obscured in most panels by the FISM symbols. Observed irradiance from the TIMED/SEE instrument is indicated by the black solid line. Data from the HEUVAC (green *), FISM (red diamond), S2000 (orange squares), and the NRL (blue diamonds) irradiance models are available on all days. SRPM model irradiances derived from the Rome (rust) and Mauna Loa (aqua) observatories are shown for two values of a coronal fill factor (CFF), 1.0 (x) and 0.5 (-).

prior to those made by SDO/EVE, have inadequate coverage and wavelength resolution to use in models of the interaction of solar radiation with the thermosphere [see, e.g., Peterson *et al.*, 2009]. To provide high spectral resolution solar irradiance values for use in aeronautical calculations several solar irradiance models have been developed to fill spectral and temporal gaps in the observations. Here we consider some of the generally used models including EUVAC [Richards *et al.*, 1994] and its higher spectral resolution

version HEUVAC [Richards *et al.*, 2006], The Flare Irradiance Spectral Model (FISM) [Chamberlin *et al.*, 2007, 2008], Solar 2000 (S2000 v2.35 [Tobiska *et al.*, 2008], <http://www.spacewx.com/solar2000.html>), the Naval Research Laboratory EUV model (NRLEUV) [Warren, 2006], and the Solar Radiation Physical Model (SRPM) [Fontenla *et al.*, 2009a, 2009b, 2011] driven by observations from the Mauna Loa Solar Observatory (MLSO) and the Solar observatory in Rome. The SRPM model has an adjustable parameter to

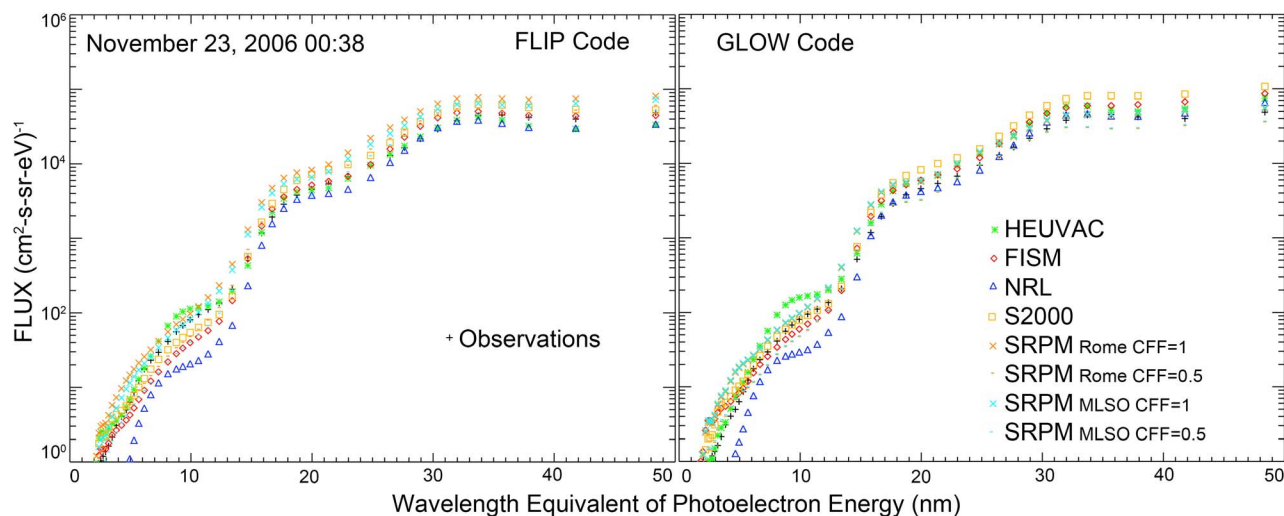


Figure 5. One-minute average observed and calculated photoelectron energy spectra. The data were acquired at 00:39 on November 23, 2006 when the FAST satellite was at an altitude of 1,700 km over the southern hemisphere on a magnetic field line that entered the ionosphere at -63° latitude and 77° west longitude and where the solar zenith angle was 81° . Data are presented as a function of the wavelength equivalent of the photoelectron energy. The observed photoelectron spectrum is indicated by plus symbols. Photoelectron spectra calculated using the (left) FLIP and (right) GLOW codes driven by the solar irradiance models shown above in Figure 4 are indicated by the symbols shown on the right.

account for uncertainties associated with modeling coronal emissions using the visible images from the MLSO or Rome observatories. Here we have used SRPM coronal filling factors (CFF) of 1 and 0.5. The HEUVAC and NRL/LEUV models are driven by the $F_{10.7}$ index; the FISM and S2000 models are driven by TIMED/SEE, and GOES X-ray observations and $F_{10.7}$ when these observations are not available.

[11] Comparison of observed photoelectron energy spectra and solar irradiance models is facilitated by considering broad wavelength bands [Peterson *et al.*, 2009]. Figure 4 presents model estimated and observed solar irradiances for the 0–7, 30–31, 0–45, 0–27, and 27–45 nm ranges. Measurements from the TIMED/SEE instrument are indicated by the solid black line in each panel. Model data are indicated by the symbols listed in the caption to Figure 4. In many cases the black line is not visible because it is identical to the FISM model and over-plotted by red diamonds. As shown in Figure 4, SRPM irradiances generated with a CFF of 0.5 are lower at all wavelengths than those generated with a CFF of 1. We note that the NRL solar irradiance model does not extend below 5 nm [Warren, 2006], accounting for the low value for the NRL irradiance over the 0–7 nm region given in Figure 4 (top).

[12] The two relatively short intervals of solar activity centered on December 6 and 12 (days 83 and 89 in Figure 4) shown in the TIMED/SEE data are associated with bursts of solar flares. We note the significant spectral differences of the irradiance models displayed in Figure 4 and calculated photoelectron spectra shown in Figure 5. The goal of this paper is to compare, on solar rotation time scales, observed photoelectron energy spectra with those calculated using the various solar irradiance models. Before we do the comparison,

we first need to describe the photoelectron production codes we are using in more detail.

4. Photoelectron Models

[13] Ionosphere/Thermosphere (I-T) codes account explicitly or implicitly for energy input from photoelectrons, but most codes are not generally available for use in independent investigations. We are aware of only two open I-T codes that are configured so that users can explicitly input various solar irradiance spectra and examine the resulting photoelectron energy spectra. These are the GLOW [Solomon and Qian, 2005, and references therein], and the Field Line Interhemispheric Plasma (FLIP) [Richards, 2001, 2002, 2004, and references therein] codes. The GLOW code is a stand-alone module available from the NCAR website (<http://download.hao.ucar.edu/pub/stans/glow/>). The FLIP model includes an updated version of the simple photoelectron production model published by Richards and Torr [1983] and is available on request from Dr. Richards. In this study, both models use the International Reference Ionosphere (IRI, <http://iri.gsfc.nasa.gov/>) and the Mass Spectrometer and Incoherent Scatter (MSIS, <http://en.wikipedia.org/wiki/NRLMSISE-00>) neutral atmosphere models to specify the state of the ionosphere-thermosphere system.

[14] Our approach to evaluating spectral uncertainties in models of solar irradiance is to analyze the differences between predicted and observed photoelectron spectra. To more clearly display the high-energy electron data most relevant to this investigation the photoelectron energy spectra are displayed as a function of the wavelength equivalent. The equivalent wavelength is calculated using a constant 15 eV ionization potential. This approximation does not take into account the production of Auger electrons

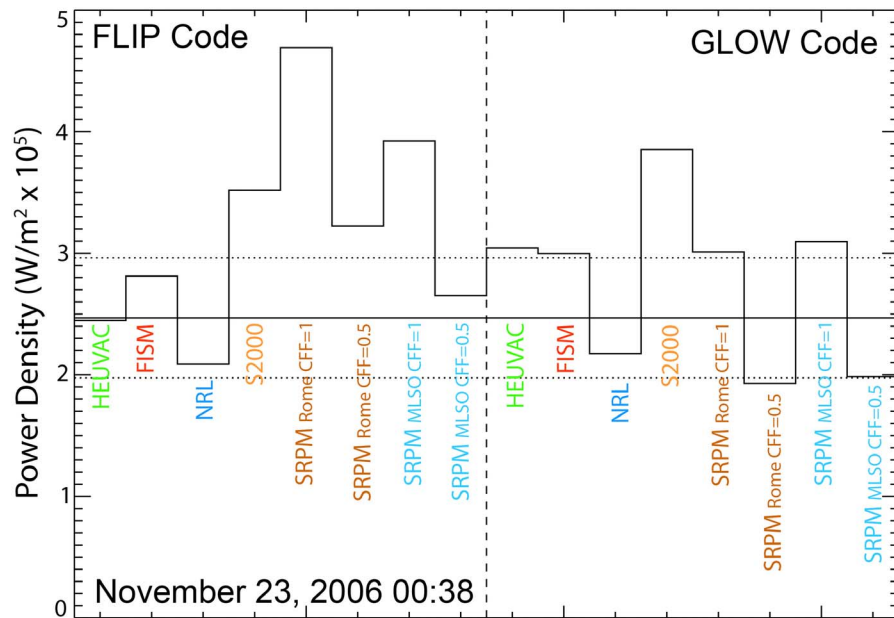


Figure 6. Estimated power density of escaping photoelectrons over the energy range 10 eV to 600 eV (2 to 45 nm equivalent wavelength) at the top of the ionosphere in units of $\text{W/m}^2 \times 10^5$ for the photoelectron spectra shown in Figure 5. The value derived from observations ($2.5 \times 10^{-5} \text{ W/m}^2$) is indicated by the solid horizontal line. Values calculated from the FLIP (GLOW) code and the indicated solar irradiance models appear to the left (right) of the vertical dashed line. The two horizontal dotted lines indicate $\pm 20\%$ of the observations (see text). The solar irradiance models and colors used to designate them are the same as those used in Figure 5.

from atomic oxygen or molecular nitrogen which have energies above 250 eV [Richards *et al.*, 2006; Peterson *et al.*, 2009]. Photoelectron energy spectra as a function of equivalent wavelength from the code and solar irradiance model pairs used in this investigation are shown in Figure 5 for the one-minute period identified in the caption. The predicted and observed photoelectron spectra agree within an order of magnitude for this interval.

[15] Another measure of differences between observed and predicted photoelectron energy spectra is the power density of the escaping photoelectron energy flux. This quantity is obtained by integrating the energy flux of escaping photoelectrons over a specified equivalent wavelength range and expressing it in the same units as solar irradiance, W/m^2 . Figure 6 presents estimated power density of the escaping photoelectrons at the top of the ionosphere over the energy range 10 eV to 600 eV (2 to 45 nm equivalent wavelength) derived from the data presented in Figure 5. Values calculated from the FLIP (GLOW) code appear in the left (right) of the vertical dashed line. The eight solar irradiance models and colors used to designate them are the same as those used in Figures 5 and 6. The photoelectron power density derived from observations ($2.5 \times 10^{-5} \text{ W/m}^2$) is indicated by the solid horizontal line. The two dotted horizontal lines, at $\pm 20\%$ of the value derived from observations, indicate the estimated 40% uncertainty in the observations [Woods *et al.*, 2003].

[16] Figure 6 shows that the power density of escaping photoelectrons is within observational uncertainties for most model pairs for this energy range and time. However, Figure 4 shows significant variation in solar irradiance as a

function of wavelength and Figure 5 shows considerable variation in the agreement between observed and modeled escaping photoelectron fluxes as a function of equivalent wavelength. To investigate the equivalent wavelength dependence of the relatively small differences between the observations and the code / irradiance pair predictions, we display the relative differences between observed and calculated photoelectron energy spectra in Figure 7. Here we define the relative difference as (observations – model) / model. The data presented in Figure 5 have been used to calculate the relative differences reported in Figure 7. Data below 2 nm are not shown in Figure 7 because the observed photoelectron fluxes are below the instrumental sensitivity.

[17] The relative differences in Figure 7 originate from the differences in solar irradiance spectra, the different ways solar irradiance spectra are binned and processed in the two codes, and the possibly different atomic cross sections used in the two codes. We use the differences in the photoelectron spectra produced by two codes with the same inputs to estimate uncertainties associated with calculated photoelectron spectra. The default solar irradiance spectra used by the two codes are very similar; they differ primarily in their spectral resolution. The GLOW-EUVAC default solar irradiance model was optimized to provide best overall agreement with soft X-ray observations from the Student Nitric Oxide Explorer (SNOE) spacecraft [Bailey *et al.*, 2002]. The FLIP-HEUVAC default solar irradiance model was optimized to provide best overall agreement with photoelectron energy spectra observed on the Atmosphere Explorer, Dynamics Explorer, and Fast Auroral Snapshot (FAST) satellites [Richards *et al.*, 2006]. The version of the EUVAC

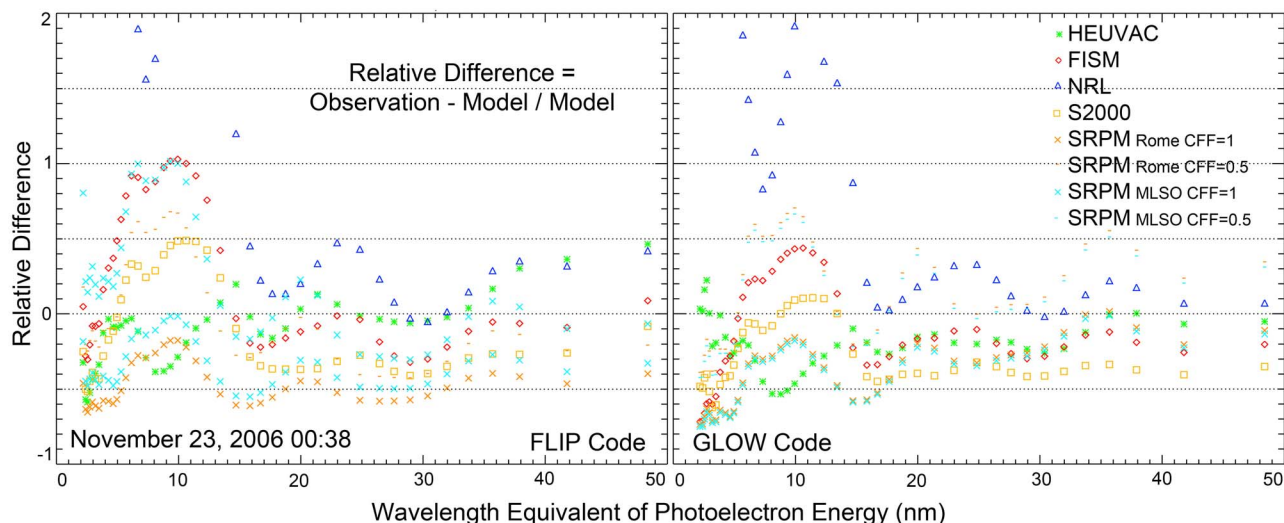


Figure 7. Relative differences between observed and modeled photoelectron spectra presented in Figure 5 as a function of the wavelength equivalent of the photoelectron energy. Relative differences between observations and values calculated using the (left) FLIP and (right) GLOW codes driven by the various solar irradiance are indicated by the symbols shown in Figure 5 (right). Data below 2 nm are not shown because the one-minute average of the observed photoelectron flux is below the detector sensitivity level.

solar irradiance model used in the GLOW code has 1 nm resolution above 6 nm. It also includes some narrow band emissions below 5 nm [Solomon *et al.*, 2001; Bailey *et al.*, 2002]. The version of the FLIP code used here uses uniformly spaced, 1 nm resolution, solar irradiance spectra. We used 1 nm resolution for the solar irradiance models in the FISM code and converted to the EUVAC bins for use with the GLOW code.

[18] To explore differences between the GLOW and FLIP codes, we compare observed photoelectron spectra for the interval shown in Figures 5 and 7 with those calculated with the FLIP/HEUVAC, GLOW/HEUVAC, and GLOW/EUVAC model pairs in Figure 8. The FLIP/HEUVAC and

GLOW/EUVAC model pairs are the ‘native’ modes of the two codes. The GLOW/HEUVAC model pair uses the HEUVAC irradiance model converted into non-uniformly spaced spectral bins below 6 nm used by the GLOW code. We use the relative difference format of Figure 7 to display the relative difference of the photoelectron flux calculated using the indicated code/model pairs in Figure 8a. Figure 8b displays the differences between the HEUVAC and EUVAC solar irradiance model spectra as a function of wavelength for this interval.

[19] Comparison of photoelectron spectra produced by the same code, but with different solar irradiance models are shown by the solid line in Figure 8a. The solid line in

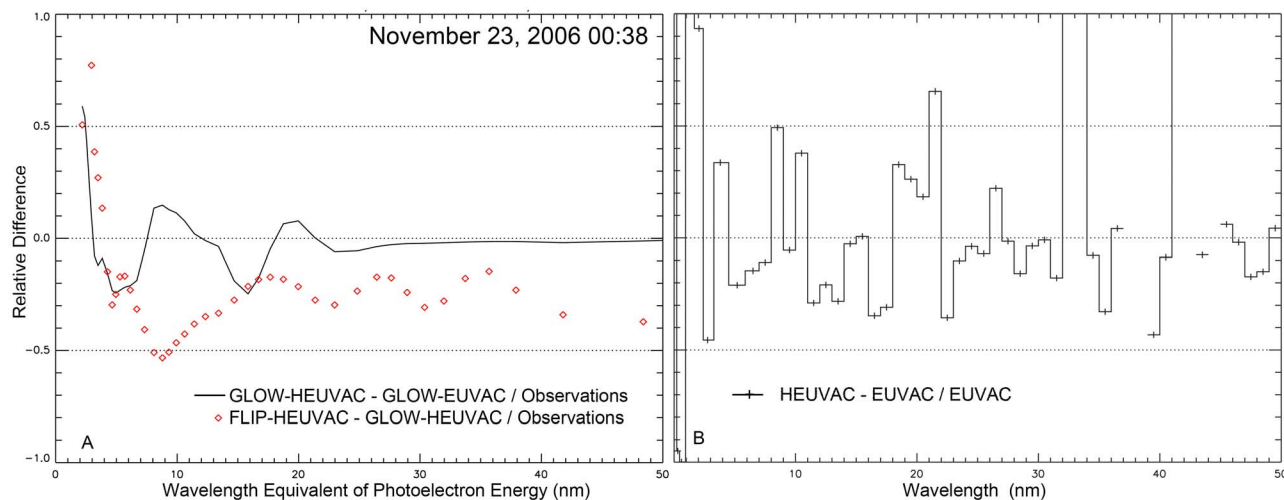


Figure 8. (a) Relative differences between calculated photoelectron energy spectra calculated with the FLIP/HEUVAC, GLOW/HEUVAC, and GLOW/EUVAC model pairs (see text). (b) Relative difference between the HEUVAC and EUVAC solar irradiance models as a function of Wavelength. Figures 8a and 8b show results for 00:38 on November 23, 2006.

Figure 8a illustrates the primary difference between photoelectron spectra calculated by the native EUVAC and imported HEUVAC solar irradiance models by the GLOW code. For equivalent wavelengths greater than ~ 25 nm (i.e., photoelectrons with energies below ~ 33 eV) the differences are insignificant. The significant differences in solar irradiance above 31 nm between the HEUVAC and EUVAC solar irradiance spectra seen in Figure 8b are not seen in the photoelectron energy spectra calculated by the GLOW code. This reflects the fact that solar irradiance above the intense HeII 30.4 nm line does not produce a significant photoelectron flux. The photoelectron energy spectrum below 20 eV (31 nm equivalent wavelength) is dominated by so-called cascade electrons produced when more energetic photoelectrons suffer inelastic collisions with thermospheric neutrals [e.g., *Peterson et al.*, 2009, Figure 11]. Below ~ 25 nm the variations in the calculated photoelectron number flux calculated by the GLOW code from the two solar irradiance models indicated by the solid line Figure 8a are strongly correlated with the relative differences in the HEUVAC and EUVAC solar irradiance models shown in Figure 8b. The correlation is not stronger because of the energy resolution of the FAST electron detector and contributions from cascade electrons.

[20] The red symbols in Figure 8a show the systematic differences in photoelectron energy spectra produced by the FLIP and GLOW codes using the same HEUVAC solar irradiance model. The GLOW code predicts more intense photoelectron fluxes above ~ 5 nm (below ~ 105 eV) and less intense fluxes below ~ 5 nm. Above about 20 nm (below ~ 45 eV) the GLOW code predicts a photoelectron flux $\sim 25\%$ higher than that predicted by the FLIP code for the same solar irradiance input for this particular day and solar irradiance model. We note that, above ~ 5 nm equivalent wavelength, that the difference between the FLIP and GLOW calculations are comparable to the observational uncertainties of $\pm 20\%$.

[21] Uncertainties also arise in the calculated photoelectron distributions from uncertainties in the neutral and ionized atmospheres. Limitations of the IRI and MSIS empirical models used in both the FLIP and GLOW codes have been widely discussed. See, e.g., *Richards et al.* [2010], *Picone et al.* [2002], and *Lühr and Xiong* [2010] for discussions on the strengths and weaknesses of the IRI and MSIS models. However, uncertainties in the neutral composition in the topside ionosphere, where the escaping photoelectrons originate, have a negligible effect on the calculated photoelectron energy spectra. As noted by *Richards and Peterson* [2008], the escape photoelectron flux is not sensitive to neutral composition because atomic oxygen is the dominant neutral species at escape altitudes and both the production and loss of photoelectrons are proportional to atomic oxygen. Even where molecular nitrogen is important, the photoelectron flux is not particularly sensitive to composition at most energies because the ratio of production frequencies is similar to the ratio of the electron impact cross sections for O and N₂ [*Richards and Torr*, 1985]. Below 20 eV, the escaping flux is sensitive to the electron density because of energy degradation through Coulomb collisions.

[22] It is important to recognize that the comparisons between observed and modeled photoelectron energy spectra presented in Figures 5, 6, 7, and 8 are only valid for the solar

spectral irradiance that existed at 00:38 on November 23, 2006. For this interval we conclude that uncertainties in photoelectron spectra calculated using the GLOW and FLIP codes are comparable to the $\pm 20\%$ uncertainty in the observations.

5. Photoelectron Spectra Observed From September 14, 2006 to December 31, 2006

[23] Figure 2 above presented daily average photoelectron energy spectra obtained on the FAST satellite from the 11,969 one minute data intervals processed between September 14 and December 31, 2006. On average 110 non-uniformly spaced one-minute spectra were obtained each day, although this number varied as the sampling intervals changed with orbit orientation. The 109-day interval included four solar rotations. As noted above, the interval is characterized by modest solar and geomagnetic activity. Data were acquired at altitudes from 1,500 to 3,800 km in both hemispheres. Because of the precession of the FAST orbit, data are primarily from the northern hemisphere before November 7 and from the southern hemisphere after. Also after November 7 most of the data were acquired near the terminator where the solar zenith angle was near to but less than 90° . Note that the escaping photoelectron flux does not vary strongly with solar zenith angle near 90° . Figure 2 shows no visible signature in the photoelectron spectra of the recurring geomagnetic activity during this interval that has been extensively discussed by *Thayer et al.* [2008] and others. A detailed examination not shown here reveals no statistically significant variations in the photoelectron energy spectra with the 6- to 9-day periods reported by *Thayer et al.* [2008] and others for this interval. As noted and discussed more fully below, we have identified systematic spectral variations on solar rotation time scales in the photoelectron data shown in Figure 2.

[24] For each of the 11,969 one-minute average photoelectron spectra acquired we calculated photoelectron energy spectra using both the FLIP and GLOW codes with input from irradiance spectra calculated from each of the solar irradiance models discussed above. Inputs to these calculations included the location of the foot point of magnetic field passing through the FAST satellite as well as the appropriate solar and geomagnetic indices needed for the IRI ionospheric model, the MSIS neutral density model, and the solar irradiance models. Daily and 109-day averaged photoelectron energy spectra for each code/model pair were then calculated. There are several ways to compare observed and calculated photoelectron fluxes. Below we compare daily averaged photoelectron fluxes as a function of energy and photoelectron power densities over specific wavelength equivalent energy ranges for the full interval.

[25] We first examine the average differences over the full interval. Figure 9 presents the 109-day average relative differences between observed and modeled photoelectron fluxes. Most of the code/model pairs have average relative differences between -0.5 and $+0.5$ for most equivalent wavelengths. The major exception is for equivalent wavelengths below ~ 15 nm where many code model pairs produce photoelectron number fluxes significantly below the observations. Figure 9c shows that above about 15 nm the photoelectron number flux produced by the GLOW code is

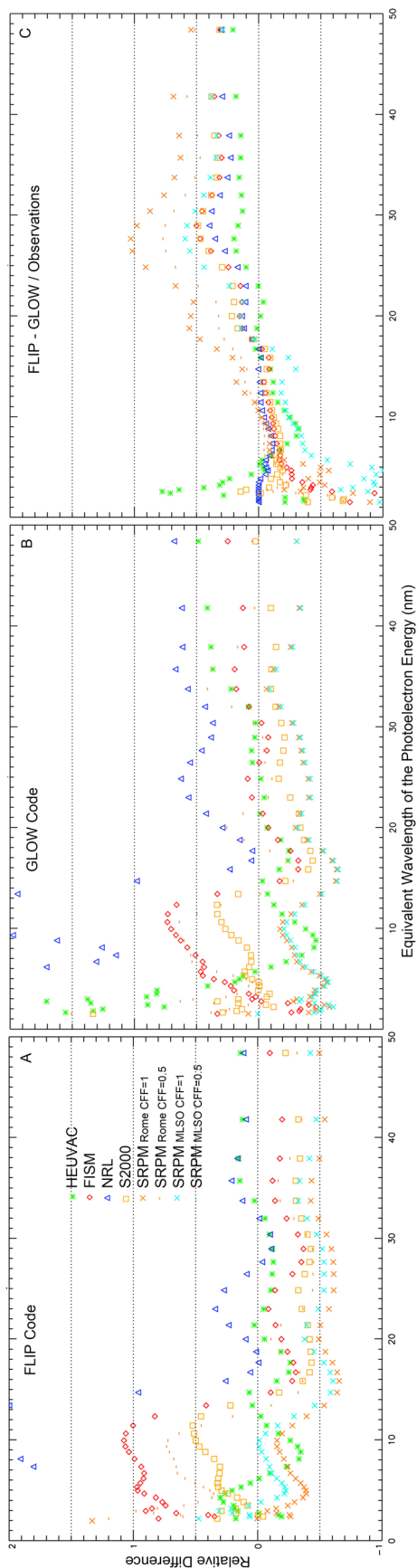


Figure 9. Relative difference between the average observed and calculated photoelectron energy spectra over the 109-day interval for the 8 solar irradiance models and the FLIP and GLOW photoelectron production codes. (a, b) Average observations – average calculation / average calculation (c) average FLIP calculation – average GLOW calculation / average observations. The symbols and colors for the solar irradiance models used are the same as those used in Figures 5 and 7.

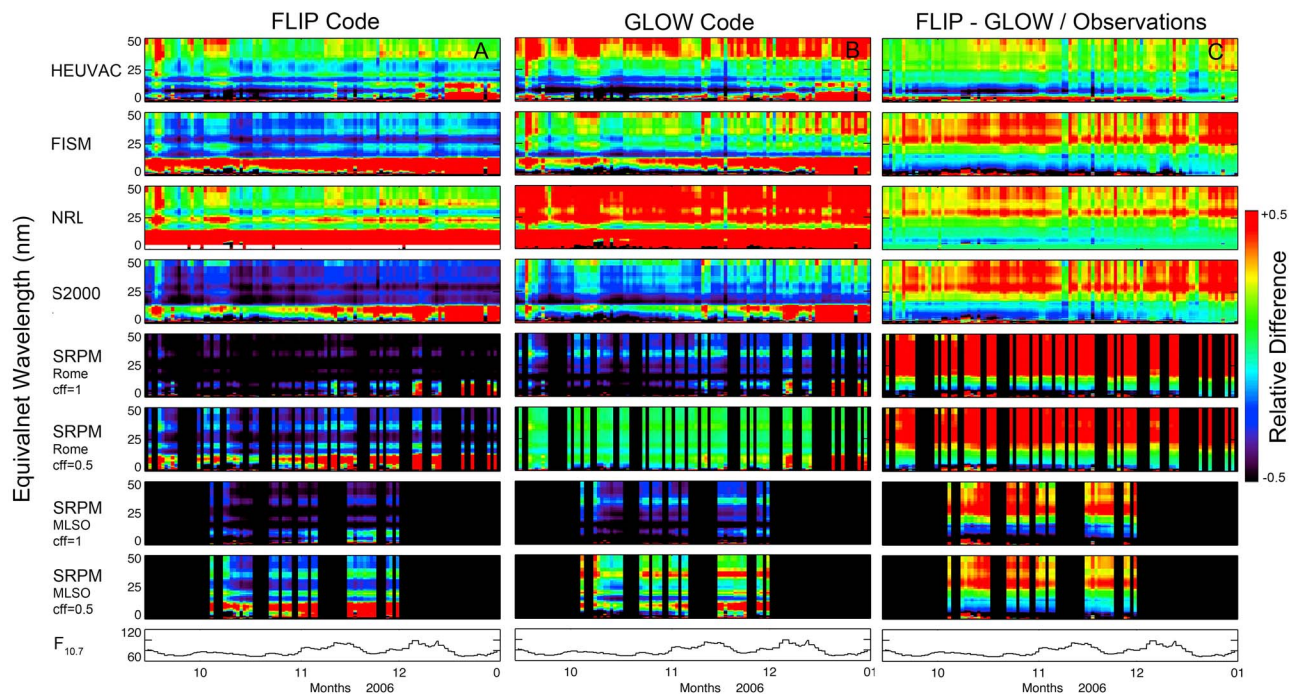


Figure 10. Daily average relative difference between observed and calculated photoelectron energy spectra in spectrogram format. Data are presented for the 109-days between September 14 and December 31, 2006. (a, b) Relative difference is defined as (observed energy spectrum – calculated energy spectrum) / (calculated energy spectrum) using the FLIP and GLOW codes respectively. (c) Relative difference is defined as (calculated with FLIP – calculated with GLOW) / Observed spectrum. Data values are presented over the equivalent wavelength range from 0 to 50 nm. The relative difference from -0.5 to 0.5 is encoded using the color bar on the right. See text for descriptions of the eight solar irradiance models indicated on the left. The daily $F_{10.7}$ solar index is given at the bottom for reference.

systematically lower than that produced by the FLIP code using the same solar irradiance model, between ~ 5 and ~ 15 nm the FLIP code produces fluxes systematically lower than the GLOW code. The average difference between the fluxes calculated by the two codes is below $\sim 25\%$ for most code/model pairs, which is comparable to the uncertainty in the observations.

[26] Figure 10 presents the relative difference between the daily averaged photoelectron flux observations shown in Figure 2 and those calculated from each of the 16 code/model pairs we are examining. Figure 10 also displays the solar $F_{10.7}$ index for reference. In this format a constant color in Figures 10a and 10b indicates that the energy dependence of the observed and calculated photoelectron energy spectrum are nearly identical. In Figure 10c green indicates that the energy dependence of the photoelectron energy spectra calculated using the GLOW and FLIP codes using the solar irradiance model indicated on the left are equal. Red indicates that the calculated values are more than 50% lower than observations (Figures 10a and 10b) or that the FLIP calculation is more than 50% greater relative to observations than the GLOW calculation (Figure 10c). Green indicates that the relative difference between photoelectron fluxes produced by the code/model pair and observations is zero. Solid black for calculations using the SRPM irradiance model indicate that no observatory data were available on that day to calculate the SRPM irradiance spectra. Isolated

black patches in Figure 10 indicate that the calculated photoelectron flux is more than 50% higher than what is observed. We note that the observed photoelectron flux shown in Figure 2 and the relative number flux differences shown in Figures 10a and 10b show a very weak correspondence to variations in the daily $F_{10.7}$ solar index.

[27] To gain insight into thermospheric heating, and to more clearly identify spectral and temporal variations in the observed photoelectron flux we next examine the relationship between the total ionizing radiation power and the power in the escaping flux of photoelectrons displayed in Figures 9 and 10. Integrated photoelectron energy flux over the equivalent wavelength range from 2 to 45 nm is a good measure of the escaping photoelectron power density; it has the units of W/m^2 . Figure 11 presents observed and calculated daily average partial photoelectron power density for 109 days beginning on September 14, 2006. The black dotted lines in Figure 11 indicate the observational uncertainty of $\pm 20\%$ of the observed value [Woods *et al.*, 2003]. Table 1 compares the 109-day averaged observed and calculated photoelectron power density over the 2–45 nm equivalent wavelength range and model solar irradiance power for the code/model pairs considered above.

[28] The 109-day average of the observed photoelectron power density in the 2–45 nm equivalent wavelength range shown in Figure 11 is $3.5 \times 10^{-5} \text{ W}/\text{m}^2$. The 109-day average of solar irradiances in the 2–45 nm range calculated

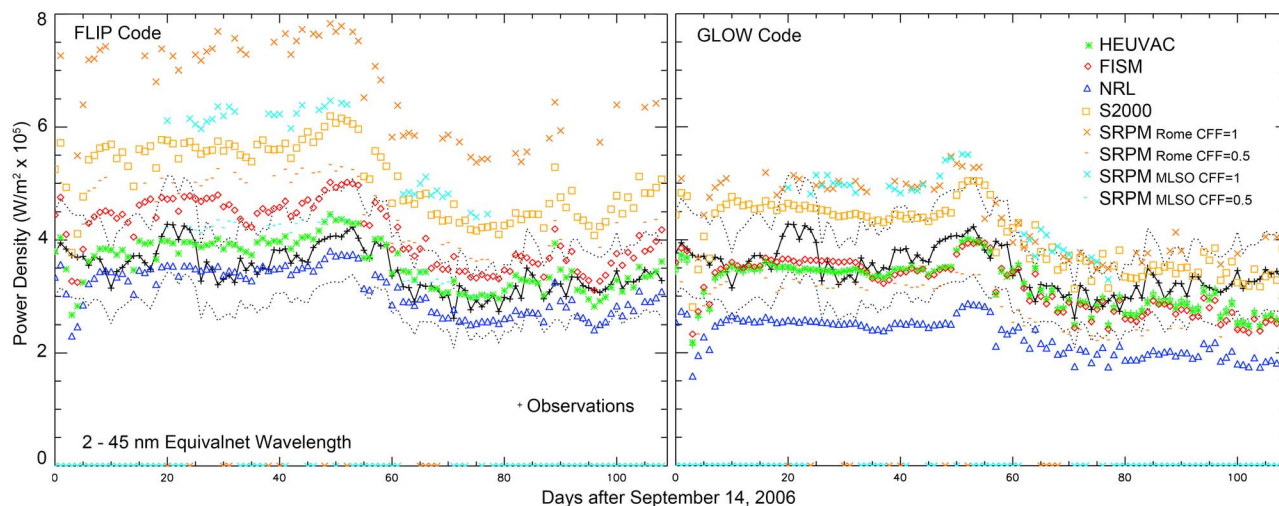


Figure 11. Estimated power density of the escaping photoelectrons over the energy range 10 eV to 600 eV (2 to 45 nm equivalent wavelength) at the top of the ionosphere in units of $W/m^2 \times 10^5$ for the 109 days between September 14 and December 31, 2006. The values derived from observations is indicated by the solid line and appears in both panels. Values calculated from the FLIP (GLOW) code and the indicated solar irradiance models appear in the left (right) panels. The two dotted lines in each panel indicate $\pm 20\%$ of the observations (see text). The solar irradiance models and colors used to designate them are the same as those used above.

from data presented in Figures 4 and 5 and displayed in column 2 of Table 1 is $2.44 \times 10^{-3} W/m^2$. This is about 1.7% of the estimated solar irradiance in the same wavelength range (columns 3 and 4 of Table 1). The fraction of modeled solar irradiance power seen in escaping photoelectrons varies from 1.1% (GLOW/SRPM driven by Rome observations and a coronal fill factor of 1.0) to 2.3% (FLIP/NRL). The ratio of the average calculated to average observed photoelectron power density over 2–45 nm equivalent wavelength range shown in columns 5 and 6 of Table 1 is ~ 1.11 . This ratio varies from 66% (GLOW/NRL) to 194% (FLIP driven by Rome observations and a coronal fill factor of 1). The average photoelectron power calculated using FLIP is $133 \pm 12\%$ of the observed photoelectron power over the 2–45 nm range compared to $88 \pm 18\%$ calculated by the GLOW code. The differences between observed and modeled photoelectron power over the full photoelectron energy range (2 to 45 nm equivalent wavelength) are comparable to the $\pm 20\%$ uncertainties in the observations.

[29] To analyze the equivalent wavelength dependence of observed and calculated photoelectron spectra Peterson *et al.* [2009] found that it was instructive to consider five specific equivalent wavelength ranges. Here we compare integrated photoelectron energy flux (i.e., photoelectron power density) over selected bands. Table 2 presents the 109-day average observed and calculated photoelectron power density shown in the selected equivalent wavelength bands used by Peterson *et al.*

[30] We conclude from the data presented above that the solar irradiance models investigated adequately reproduce the average solar energy input to the thermosphere over the 109 day interval examined. For the SRPM model the coronal filling factor of 0.5 best reproduces the average photoelectron observations.

[31] We now turn our attention to variability on solar rotation time scales. This variability is visible in the format of Figure 12. Figure 12 presents the observed daily averaged photoelectron power density in the 5 equivalent wavelength bands and the relative difference from the average values as a function of time. The relative difference in Figure 12b is defined as the (daily observation – average observation) / average observation. As shown above in Figure 2, the absolute intensity of observed photoelectron fluxes decreased after November 7 because of the precession of the FAST orbit. This shift in intensity is noticeable in Figures 12a and 12b. Nevertheless relative differences shown in Figure 12b show spectral and solar rotation time scale variations in the escaping photoelectron power density, not all of which is captured by variations in the solar $F_{10.7}$ index. Photoelectron power density variations observed in the solar rotation that peaked in early October, are most prominent in the higher

Table 1. Comparison of Modeled and Observed Power^a

Irradiance Model (2–45 nm)	Photoelectron Power / Irradiance		Calculated/Observed Photoelectron Power		
	FLIP	GLOW	FLIP	GLOW	
HEUVAC	2.05e-03	0.018	0.016	1.04	0.92
FISM	2.01e-03	0.021	0.016	1.19	0.91
NRL	1.33e-03	0.023	0.017	0.90	0.66
S2000	2.54e-03	0.020	0.016	1.47	1.17
ROME cff = 1	4.00-03	0.017	0.011	1.94	1.29
ROME cff = 0.1	2.42e-03	0.019	0.012	1.32	0.83
MLSO cff = 1	3.24e-03	0.017	0.014	1.64	1.33
MSLO cff = 0.5	1.96e-03	0.020	0.015	1.12	0.85

^aComparison of average solar irradiance in the 2–45 nm range with calculations of photoelectron power density for the 109-day interval at the end of 2006 shown in Figure 11.

Table 2. Observed and Calculated Average Photoelectron Power Density in W/m^2 for the 109 Days Between September 14 and December 31, 2006^a

Band (nm)	FLIP Code					GLOW Code				
	2–4	4–8	10–16	18–27	27–45	2–4	4–8	10–16	18–27	27–45
OBS	2.94e-07	3.57e-07	8.50e-07	5.62e-06	1.91e-05					
HEUVAC	2.82e-07	3.48e-07	8.73e-07	6.04e-06	1.86e-05	1.43e-07	3.79e-07	9.56e-07	5.84e-06	1.56e-05
FISM	1.78e-07	1.85e-07	7.83e-07	6.71e-06	2.45e-05	3.34e-07	2.53e-07	8.45e-07	5.61e-06	1.75e-05
NRL	5.60e-10	8.04e-08	3.93e-07	4.66e-06	1.82e-05	4.38e-10	1.08e-07	4.00e-07	3.83e-06	1.25e-05
S2000	2.64e-07	2.76e-07	8.94e-07	9.01e-06	2.91e-05	2.86e-07	3.36e-07	9.55e-07	7.61e-06	2.19e-05
ROME cff = 1	3.66e-07	5.32e-07	1.96e-06	1.29e-05	3.92e-05	5.11e-07	6.25e-07	1.85e-06	8.88e-06	2.52e-05
ROME cff = 0.5	1.71e-07	2.36e-07	1.03e-06	8.38e-06	2.78e-05	2.31e-07	2.74e-07	9.58e-07	5.58e-06	1.68e-05
MLSO cff = 1	2.57e-07	4.29e-07	1.70e-06	1.07e-05	3.36e-05	5.39e-07	6.46e-07	1.91e-06	9.12e-06	2.57e-05
MSLO cff = 0.5	1.19e-07	1.89e-07	8.98e-07	7.00e-06	2.39e-05	2.43e-07	2.83e-07	9.89e-07	5.73e-06	1.71e-05

^aObserved (OBS) values and those calculated with the FLIP and GLOW codes using the indicated solar irradiance models are given for the five equivalent wavelength bands.

equivalent wavelength bands, indicative of variations in solar flux above ~ 20 nm. These variations are related to the passage of multiple active regions across the solar disk that can be seen in images from the Solar and Heliospheric Observatory (SOHO) Extreme ultraviolet Imaging Telescope (EIT, <http://umbra.nascom.nasa.gov/eit/> not shown here). The solar rotation that peaked in early December shows significant photoelectron power density in the lowest equivalent wavelength bands indicative of solar irradiance below ~ 15 nm. The solar rotation that peaked in early November had a more complex signature in both the observed relative difference in power density and the $F_{10.7}$ index. We note that the solar rotation signature seen in the band-integrated format of Figure 12a is only slightly more prominent than it is in Figure 2 and that a $>50\%$ variation in irradiance below 20 nm

on solar rotation time scales is not unusual [*Chamberlin et al.*, 2007, 2008].

[32] Figure 13 presents the relative difference between observed and calculated daily average photoelectron power density for the five wavelength bands shown in Table 2 and Figure 12. Figure 13 reproduces the data in Figures 10a and 10b with lower resolution in equivalent wavelength. The solar rotation signature seen in Figures 2 and 12a is not as detectable in the differences between observed and modeled photoelectron fluxes in Figure 10 or in the band-integrated format of Figure 13. This is because none of the model photoelectron fluxes calculated with code/model pairs considered show comparable variations on solar rotation time scales. Table 3 presents ratios of observed and calculated photoelectron power density for two periods and the five

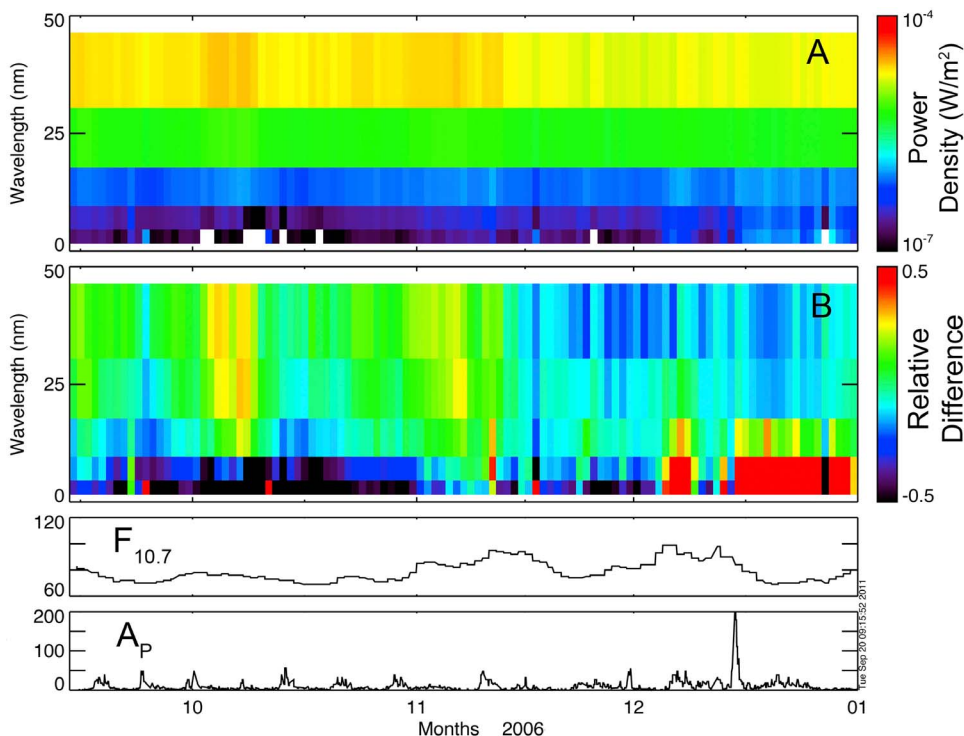


Figure 12. (a) Observed daily averaged photoelectron power density in the 5 equivalent wavelength bands given in Table 2 as a function of time. The power density in units of W/m^2 is encoded by the color bar on the right. (b) Relative difference between the observed and average power density for the data shown in Figure 12a. The solar $F_{10.7}$ and magnetic A_p indices are reproduced in the bottom two panels.

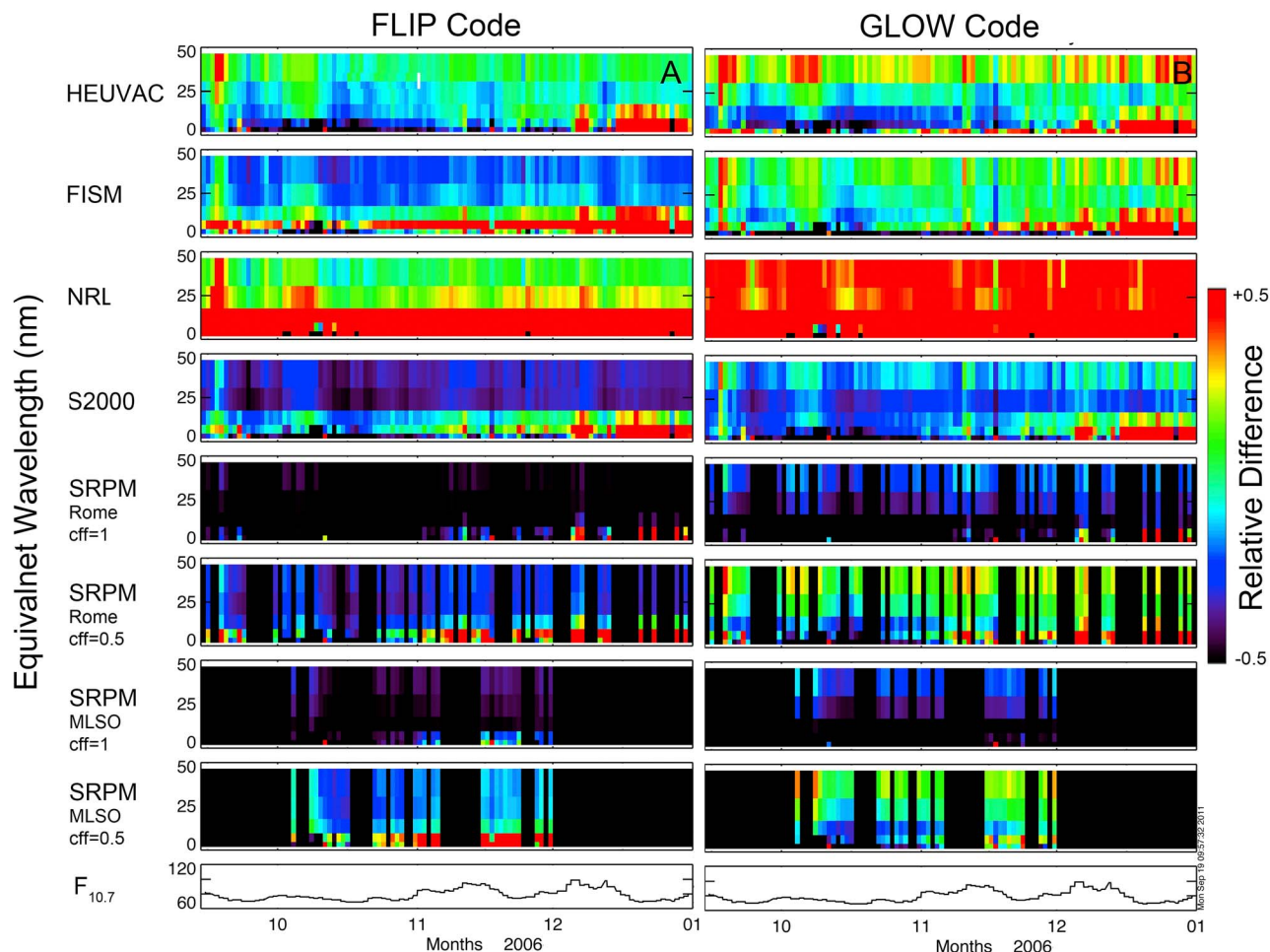


Figure 13. Daily average relative differences between calculated and observed photoelectron power density for the five equivalent wavelength bands identified in Table 2 in spectrogram format. Data are presented for the 109 days between September 14 and December 31, 2006. Relative difference b is defined as $(\text{observed power density} - \text{calculated power density}) / (\text{calculated power density})$ using the FLIP and GLOW codes respectively. The relative difference from -0.5 to 0.5 is encoded using the color bar on the right. See text for descriptions of the eight solar irradiance models indicated on the left. The daily $F_{10.7}$ solar index is given at the bottom for reference.

indicated equivalent wavelength bands. The two intervals were chosen for the largest variations in the 20 to 45 nm equivalent energy range (September 30 to October 10) and intervals with the largest and smallest photoelectron power density in the 2–4 nm equivalent wavelength bands. The observational data for September 30 to October 10 shown in Table 3 show a 10–30% variation in the photoelectron power density for all but the 2–4 nm range where the observed data are below the instrumental threshold. None of the code/model pairs reproduce these variations. The ratio of the average photoelectron power density observed from December 19 to 26 compared to that observed from September 14 and 21 is larger than 1 for the three lowest wavelength bands considered and less than 1 for the other two. For equivalent wavelengths below ~ 16 nm the code/model pairs considered do not capture any of the variation on solar rotation time scales. The magnitude of the variations in photoelectron flux seen in Figure 12 and power density in Table 3 is comparable to the variation in solar irradiance in

the 1–50 nm range over solar rotation time scales reported by Chamberlin *et al.* [2007, Figure 9] and others.

[33] In the next sections we analyze the data from the 109 day interval in late 2006 to see what the differences between photoelectron observations and the photoelectron fluxes calculated using the code/model pairs can tell us about the reliability of solar irradiance models on solar rotation time scales. But first we must consider systematic differences between photoelectron fluxes calculated by the FLIP and GLOW codes which we use here to estimate the uncertainties in the modeled photoelectron fluxes.

5.1. Photoelectron Fluxes Calculated Using the FLIP and GLOW Codes Compared

[34] The FLIP and GLOW code calculated photoelectron power densities over the 2–45 nm equivalent wavelength range in Figure 11 and Table 1 generally agree. The systematically lower photoelectron fluxes observed after November 7 are reproduced quite well by most code/model

Table 3. Ratio of Observed and Modeled Photoelectron Power in Five Equivalent Wavelength Bands for Selected Intervals^a

Band Range (nm)	October 3–9 / Seven Days Before and After					December 19–26 / September 14–21				
	2:4	4:8	10:16	18:27	27:45	2:4	4:8	10:16	18:27	27:45
Observations	-	1.08	1.2	1.29	1.21	5.08	2.63	1.29	0.83	0.76
FLIP										
HEUVAC	1.02	1.01	1.01	1.01	1.01	0.83	0.91	0.91	0.91	0.87
FISM	1.02	1.01	1.01	1.01	1.01	0.68	0.79	0.93	0.93	0.84
NRL	1.02	0.95	0.99	1.01	1.02	0.90	0.92	0.91	0.90	0.86
S2000	1.02	1.03	1.02	1.01	1.02	0.86	0.91	0.92	0.92	0.89
Rome cff = 1	1.00	1.00	1.00	1.00	0.99	0.91	0.93	0.92	0.92	0.89
Rome cff = 0.5	1.00	1.00	1.00	1.00	0.99	0.91	0.93	0.92	0.92	0.88
MLSO cff = 1	1.00	1.00	1.00	1.00	0.99	-	-	-	-	-
MLSO cff = 0.5	1.00	1.00	1.00	1.00	0.99	-	-	-	-	-
GLOW										
HEUVAC	1.02	1.00	1.00	1.00	0.99	0.95	0.92	0.89	0.90	0.82
FISM	1.03	1.02	1.00	1.00	1.00	0.70	0.80	0.89	0.90	0.75
NRL	1.00	1.00	1.00	1.00	1.00	0.92	0.91	0.88	0.89	0.80
S2000	1.02	1.03	1.01	1.00	1.01	0.92	0.91	0.89	0.89	0.81
Rome cff = 1	1.03	1.02	1.01	1.01	1.00	0.80	0.85	0.85	0.84	0.76
Rome cff = 0.5	1.03	1.02	1.01	1.01	1.01	0.81	0.85	0.85	0.84	0.77
MLSO cff = 1	0.99	0.99	0.99	0.99	0.99	-	-	-	-	-
MLSO cff = 0.5	1.00	1.00	1.00	1.00	0.99	-	-	-	-	-

^aThe seven days before and after October 3–9 included in the averages are September 30 to October 2 and October 10–12.

pairs. The differences for the various code/model pairs are similar to those seen between calculated photoelectron fluxes reported in Figures 10, 11, and 13. These figures show that both the FLIP and GLOW codes produce photoelectron energy spectra that agree with observations within observational uncertainties ($\pm 20\%$). Some specific and systematic differences between the results of the FLIP and GLOW codes are illustrated in Figures 8a, 9c and 10c. Figure 8a shows that the photoelectron flux calculated by the GLOW/HEUVAC model pair is greater than that calculated by the FLIP/HEUVAC model pair for equivalent wavelengths above approximately 5 nm for a one-minute interval on November 23rd. The 109-day average of the daily averaged FLIP/HEUVAC and GLOW/HEUVAC photoelectron energy spectra (Figures 9c and 10c) show that the FLIP/HEUVAC model pair produces slightly larger photoelectron fluxes at equivalent wavelengths above ~ 25 nm. Below 5 nm the comparison between calculations using the FLIP and GLOW codes is less clear, no doubt because of the highly variable and unpredictable nature of solar irradiance in this region. This region is difficult to model because the Auger cross-sections are much narrower than the resolution of the solar spectra. Thus, how the solar fluxes are assigned to the 2–3 nm Auger range is a source of uncertainty in the codes. We note that the differences between GLOW and FLIP photoelectron fluxes seen in Figures 9c and 10c are generally less than 50%, except below approximately 5 nm equivalent wavelength and for calculations using the SRPM solar irradiance spectra driven by observations from Rome with a coronal filling factor of 1. We note that on solar rotation time scales, the data in Table 3 show that the photoelectron power density calculated by the FLIP and GLOW codes agrees for all solar irradiance models used. However, the code/model pairs do not reproduce the variation in photoelectron power density on solar rotation time scales. We conclude that the differences between photoelectron spectra calculated by the FLIP and GLOW codes are generally comparable to photoelectron observational uncertainties.

5.2. Solar Irradiance Models Compared

[35] In spite of the quite dissimilar spectral character of the various solar irradiance models seen in Figure 4, the overall agreement between observed and modeled photoelectron fluxes shown in Figures 10a, 10b, 11, and 13 is good ($\pm 50\%$) and, on average, comparable to observational uncertainties above about 16 nm equivalent wavelength. Figure 12b and Table 3 show that, on solar rotation time scales, observed spectral variations in escaping photoelectron power density are larger than the observational uncertainty and the variations are not uniform in equivalent wavelength.

5.2.1. Less Than 16 nm Equivalent Wavelength

[36] All code/model pairs underestimate the photoelectron flux and power density at equivalent wavelengths shorter than ~ 16 nm (60 eV). The differences are largest below ~ 10 nm (~ 105 eV). The NRL model does not include solar irradiance below 5 nm and has the largest (both in value and temporal extent in Figures 10a, 10b and 13) relative difference with observations below 16 nm. We note that the cadence of photoelectron observations available from the FAST satellite is inadequate to follow the rapid variations in the EUV and soft X-ray region on solar flare time scales, except in unusual circumstances [e.g., Peterson *et al.*, 2008].

[37] Figure 12, shows that the escaping photoelectron power created by solar irradiance at equivalent wavelengths shorter than approximately 8 nm increased significantly from December 8 to 31, 2006 (days 84 to 109). Examination of the detailed data presented in Figure 13 indicates that after November 27 the mean difference between calculated and observed escaping photoelectron power density below 8 nm equivalent wavelength is about 1.5×10^{-6} W/m². Using the average 1.7% ratio of photoelectron power to solar irradiance calculated above and as shown in Table 1, we estimate that the solar irradiance models considered underestimated solar irradiance below 8 nm by $\sim 9 \times 10^{-5}$ W/m². Table 1 shows that the model average ionizing irradiance (from 2 to 45 nm over the 109 day interval) is 2.4×10^{-3} W/m². The

irradiance below 8 nm represents only about 4% of the average model ionizing irradiance and photoelectron power density for the 109 days, but for the interval after November 27 it is about 10 times the average modeled solar irradiance and photoelectron power density.

[38] Table 3 shows that during a solar rotation period where there is little soft X-ray irradiance for wavelengths below 16 nm all code/model pairs predict essentially no variation in photoelectron power density. The observed variation in photoelectron power however is up to 20% in the 10–16 nm equivalent wavelength band. Because the contribution of cascade electrons is not dominant below 31 nm the spectral variation in photoelectron power reflects the spectral variation in solar irradiance quite well.

[39] The underestimated irradiance power below 16 nm in the solar irradiance models inferred from photoelectron power density observations discussed above has important consequences in large-scale thermospheric models. This is consistent with earlier reports that solar irradiance in the soft X-ray range is an important and highly variable thermospheric energy source [e.g., Richards *et al.*, 1994; Bailey *et al.*, 2002; Peterson *et al.*, 2009]. As noted by Bailey *et al.* [2002] and many others, the soft X-ray ionizing radiation has a significant effect on nitric oxide chemistry and therefore thermospheric dynamics. Large-scale models that rely on the irradiance models considered here, including the data driven FISM model, systematically underestimate the variation of nitric oxide production over solar rotation time scales by sometimes by an order of magnitude.

5.2.2. Equivalent Wavelength Above 16 nm

[40] Two factors, cascade electrons and systematic differences between the FLIP and GLOW code calculations, complicate analysis above 16 nm. The nearly direct relationship between ionizing radiation below 16 nm and the resulting observed escaping photoelectron power density starts to break down above about 16 nm. As noted above, cascade electrons dominate the photoelectron energy spectrum above 31 nm equivalent wavelength. The systematic differences between photoelectron fluxes calculated using the FLIP and GLOW codes shown in Figures 9c and 10c are reflected in Table 1, which shows the photoelectron power density in the 27–45 nm band calculated using the FLIP code is greater than that calculated using the GLOW code. In Figure 13 and Tables 2 and 3, we considered two broad equivalent energy bands above 16 nm: 18–27 and 27–45 nm. Because of these complications we focus our analysis on the 18–27 nm band.

[41] On average, the code/model pairs considered reproduced the 109-day average photoelectron power density in the 18–27 nm band quite well. The generally uniform colors in Figure 13 for this band for all code/model pairs except the GLOW/NRL indicate good agreement between the observed and calculated photoelectron fluxes as a function time. Table 3 shows, however, that the observations and models differ on solar rotation time scales. For the solar rotation period from October 3–9, where there is little or no soft X-ray irradiance, the code/model pairs calculated less than 2% variation in the photoelectron power density in the 18–26 nm band compared to the 29% observed variation. For the intervals with significant soft X-ray variability (December 19–26 compared to September 14–21), the agreement between observations and calculations is as expected from

observational uncertainties. Table 3 shows that for the 18–27 nm bin, the code/model pairs predict an $89 \pm 3\%$ variation compared to the 83% observed.

5.2.3. Other Details Regarding the Agreement Between Observed and Calculated Escaping Photoelectrons

[42] The data presented above show that our technique is most sensitive to variations in solar irradiance at wavelengths shorter than ~ 31 nm (greater 24 eV equivalent energy) where so-called cascade electrons do not dominate the photoelectron energy spectrum. Table 2 shows that only the FLIP/HEUVAC model pair calculates the 109-day average photoelectron power density within observational uncertainties for all five equivalent wavelength bands considered. Four GLOW/model pairs calculate power density within the observational uncertainties for 4 of the 5 bands (HEUVAC, FISM, and the SRPM driven by both Rome and MLSO observations with a coronal filling factor of 0.5). In general the SRPM model with a coronal filling factor of 0.5 best reproduces the observed photoelectron power density reported in Figure 13 and Table 2.

[43] The four poorest model pair calculations of 109-day average photoelectron power density with calculated power density values outside observational uncertainties for all 5 energy bands are FLIP/SRPM, Rome, $\text{cff} = 1$ and GLOW/NRL and SRPM with $\text{cff} = 1$. Model pairs having power density for 4 of 5 bands outside observational uncertainties include FLIP/SRPM, $\text{cff} = 0.5$ and GLOW/SRPM, $\text{cff} = 1$.

[44] The decrease in escaping photoelectron power density associated with local minima of the $F_{10.7}$ index near September 27 and October 1 (days 14 and 35) is not well reproduced by any code/model pair for all of the equivalent wavelength ranges shown in Figure 13. The disagreement is generally greater than observational uncertainties. This confirms, yet again, that the $F_{10.7}$ index does not capture all solar XUV and EUV irradiance variability [see, e.g., Dudok de Wit *et al.*, 2009; Maruyama, 2011].

6. Summary and Conclusions

[45] We analyzed 11,969 one-minute average photoelectron energy spectra obtained during the 109 days from September 14 and December 31, 2006. During this interval geomagnetic activity was modest. The A_p index ranged from 0 to 236 with modest intensifications up to approximately 50 at regular intervals. Solar activity was moderate with the $F_{10.7}$ index ranging from 69 to 99. Four X class solar flares were observed in December. We presented the solar irradiance observations available for this interval. We considered five widely used solar irradiance models (e.g., HEUVAC, FISM, NRL, S2000, and SRPM) to fill spectral and temporal gaps in the observations. We compared observed and modeled solar irradiances in Figure 4 using the FLIP and GLOW photoelectron production codes with each of the solar irradiance models. We showed that comparison of observed and calculated escaping photoelectrons is most sensitive to variations in solar irradiance at wavelengths shorter than around 31 nm (greater 24 eV equivalent energy) where so-called cascade electrons do not dominate the photoelectron energy spectrum. We noted that uncertainties in the neutral composition in the topside ionosphere, where the escaping photoelectrons originate, have a negligible effect on the calculated photoelectron energy spectra. On average we found that

about 1.7% of the solar ionizing radiation in the range 2–45 nm was observed in the escaping photoelectron flux.

[46] Not unexpectedly, we found that the highly variable solar irradiance below 8 nm is not fully captured in any of the irradiance models considered here. This is true both for solar irradiance models driven by the $F_{10.7}$ solar radio flux (HEUVAC and NRL) and those driven by other observations and proxies (FISM, S2000, and SRPM). We estimated that the model solar irradiances were approximately 30% below those required to account for the increased photoelectron power density at equivalent wavelengths below 10 nm (above 105 eV during the modest solar activity in December 2006). During more active solar activity, Chamberlin *et al.* [2007] note that the Flare Irradiance Spectral Model (FISM) based on TIMED/SEE observations has uncertainties of $\pm 40\%$. The consequences are that large-scale models that rely on the irradiance models considered here, including the data driven FISM model, systematically underestimate the variation of nitric oxide production over solar rotation time scales. The new solar irradiance measurements from the higher temporal cadence and higher spectral resolution Extreme Ultraviolet Variability Experiment (EVE) on the Solar Dynamics Observatory (SDO) [Woods *et al.*, 2010] appear promising to resolve some of these differences in the photoelectron comparisons for the shorter wavelengths; however, SDO EVE observations did not start until 2010 and thus do not overlap with these photoelectron measurements.

[47] Considering the average photoelectron flux observed in late 2006, our results indicate that even though the solar irradiance models we considered have significantly different spectral charters, reasonable estimates of the heating effects of photoelectrons are possible with both codes except during periods of activity changes during solar rotations. We found that none of the irradiance models was much better than the others when used to calculate 109-day average escaping photoelectron power density. However, the best agreement between 109-day average observations and irradiance models was from the HEUVAC, FISM, and the SRPM with a coronal filling factor of 0.5. We note that these models are driven by the $F_{10.7}$ solar radio flux (HEUVAC) and other types of observations (FISM, EUV and XUV observations, and SRPM, solar visible images).

[48] On solar rotation time scales we find that none of the code/model pairs capture the variability of the observed photoelectron power density (or flux) within the $\pm 20\%$ observational uncertainties. During the solar rotation that peaked in early October 2006 all code/model pairs considered predicted one or two percent variation the escaping photoelectron power density in the 18 to 27 nm equivalent wavelength range (29 to 52 eV energy). FAST photoelectron observations found the variation to be 29%. For the soft X-ray region below ~ 16 nm most of the variability in escaping photoelectrons was missed. Our results indicate that existing code/model pairs, including those used in large-scale thermospheric models do not fully capture the variation of thermospheric solar energy input on solar rotation time scales.

[49] Finally we identified and documented systematic differences between photoelectron fluxes calculated using the FLIP and GLOW codes. The magnitudes of these differences were, for the most part, comparable to the observational

uncertainty of the photoelectron measurements. In any case these differences do not affect our major conclusions:

[50] 1. None of the solar irradiance models investigated completely captures the variation of solar energy input to the thermosphere on solar rotation time scales during this period.

[51] 2. All of the solar irradiance models investigated adequately reproduce the average solar energy input to the thermosphere over the 109 day interval examined.

[52] **Acknowledgments.** W.K.P. thanks Geoff Crowley, Jeff Thayer, and Jihou Lei for helpful discussions. W.K.P. was supported by NASA grant NNX12AD25G to the University of Colorado. P. G. Richards was supported by NASA grant NNX09AJ76G to George Mason University. Tom Woods is supported by NASA grant NNX07AB68G. S. C. Solomon is supported by NASA grant NNX08AQ31G to the National Center for Atmospheric Research. NCAR is sponsored by the National Science Foundation.

[53] Philippa Browning thanks the reviewers for their assistance in evaluating this paper.

References

- Bailey, S. M., C. A. Barth, and S. C. Solomon (2002), A model of nitric oxide in the lower thermosphere, *J. Geophys. Res.*, *107*(A8), 1205, doi:10.1029/2001JA000258.
- Carlson, C. W., et al. (2001), The electron and ion plasma experiment for FAST, *Space Sci. Rev.*, *98*, 33, doi:10.1023/A:1013139910140.
- Chamberlin, P. C., T. N. Woods, and F. G. Eparvier (2007), Flare Irradiance Spectral Model (FISM): Daily component algorithms and results, *Space Weather*, *5*, S07005, doi:10.1029/2007SW000316.
- Chamberlin, P. C., T. N. Woods, and F. G. Eparvier (2008), Flare Irradiance Spectral Model (FISM): Flare component algorithms and results, *Space Weather*, *6*, S05001, doi:10.1029/2007SW000372.
- Dalgarno, A., W. B. Hanson, N. W. Spencer, and E. R. Schmerling (1973), The Atmosphere Explorer mission, *Radio Sci.*, *8*, 263, doi:10.1029/RS008i004p00263.
- Doering, J. P., W. K. Peterson, C. O. Bostrom, and T. A. Potemra (1976), High resolution daytime photoelectron energy spectra from AE-E, *Geophys. Res. Lett.*, *3*, 129, doi:10.1029/GL003i003p00129.
- Dudok de Wit, T., M. Kretzschmar, J. Liliensten, and T. Woods (2009), Finding the best proxies for the solar UV irradiance, *Geophys. Res. Lett.*, *36*, L10107, doi:10.1029/2009GL037825.
- Fontenla, J. M., W. Curdt, M. Haberreiter, J. Harder, and H. Tian (2009a), Semiemperical models of the solar atmosphere III. Set of non-LTE models for far-ultraviolet/extreme-ultraviolet irradiance computation, *Astrophys. J.*, *707*, 482, doi:10.1088/0004-637X/707/1/482.
- Fontenla, J. M., E. Quémerais, I. González Hernández, C. Lindsey, and M. Haberreiter (2009b), Solar irradiance forecast and far side imaging, *Adv. Space Res.*, *44*, 457, doi:10.1016/j.asr.2009.04.010.
- Fontenla, J. M., J. Harder, W. Livingston, M. Snow, and T. Woods (2011), High-resolution solar spectral irradiance from extreme ultraviolet to far infrared, *J. Geophys. Res.*, *116*, D20108, doi:10.1029/2011JD016032.
- Garcia, H. (1994), Temperature and emission measure from GOES soft X-ray measurements, *Sol. Phys.*, *154*, 275, doi:10.1007/BF00681100.
- Kopp, G., and J. L. Lean (2011), A new, lower value of total solar irradiance: Evidence and climate significance, *Geophys. Res. Lett.*, *38*, L01706, doi:10.1029/2010GL045777.
- Lühr, H., and C. Xiong (2010), IRI-2007 model overestimates electron density during the 23/24 solar minimum, *Geophys. Res. Lett.*, *37*, L23101, doi:10.1029/2010GL045430.
- Maruyama, T. (2011), Modified solar flux index for upper atmospheric applications, *J. Geophys. Res.*, *116*, A08303, doi:10.1029/2010JA016322.
- Peterson, W. K., P. C. Chamberlin, T. N. Woods, and P. G. Richards (2008), Temporal and spectral variations of the photoelectron flux and solar irradiance during an X class solar flare, *Geophys. Res. Lett.*, *35*, L12102, doi:10.1029/2008GL033746.
- Peterson, W. K., E. N. Stavros, P. G. Richards, P. C. Chamberlin, T. N. Woods, S. M. Bailey, and S. C. Solomon (2009), Photoelectrons as a tool to evaluate spectral variations in solar EUV irradiance over solar cycle time scales, *J. Geophys. Res.*, *114*, A10304, doi:10.1029/2009JA014362.
- Picone, J. M., A. E. Hedin, D. P. Drob, and A. C. Aikin (2002), NRLMSISE-00 empirical model of the atmosphere: Statistical comparisons and scientific issues, *J. Geophys. Res.*, *107*(A12), 1468, doi:10.1029/2002JA009430.

- Richards, P. G. (2001), Seasonal and solar cycle variations of the ionospheric peak electron density: Comparison of measurement and models, *J. Geophys. Res.*, *106*, 12,803, doi:10.1029/2000JA000365.
- Richards, P. G. (2002), Ion and neutral density variations during ionospheric storms in September 1974: Comparison of measurement and models, *J. Geophys. Res.*, *107*(A11), 1361, doi:10.1029/2002JA009278.
- Richards, P. G. (2004), On the increases in nitric oxide density at midlatitudes during ionospheric storms, *J. Geophys. Res.*, *109*, A06304, doi:10.1029/2003JA010110.
- Richards, P. G., and W. K. Peterson (2008), Measured and modeled backscatter of ionospheric photoelectron fluxes, *J. Geophys. Res.*, *113*, A08321, doi:10.1029/2008JA013092.
- Richards, P. G., and D. G. Torr (1983), A simple theoretical model for calculating and parameterizing the ionospheric photoelectron flux, *J. Geophys. Res.*, *88*, 2155, doi:10.1029/JA088iA03p02155.
- Richards, P. G., and D. G. Torr (1985), The altitude variation of the ionospheric photoelectron flux: A comparison of theory and measurement, *J. Geophys. Res.*, *90*(A3), 2877, doi:10.1029/JA090iA03p02877.
- Richards, P. G., J. A. Fennelly, and D. G. Torr (1994), EUVAC: A solar EUV flux model for aeronomic calculations, *J. Geophys. Res.*, *99*, 8981, doi:10.1029/94JA00518.
- Richards, P. G., T. N. Woods, and W. K. Peterson (2006), HEUVAC: A new high resolution solar EUV proxy model, *Adv. Space Res.*, *37*, 315, doi:10.1016/j.asr.2005.06.031.
- Richards, P. G., D. Bilitza, and D. Voglozin (2010), Ion density calculator (IDC): A new efficient model of ionospheric ion densities, *Radio Sci.*, *45*, RS5007, doi:10.1029/2009RS004332.
- Solomon, S. C., and L. Qian (2005), Solar extreme-ultraviolet irradiance for general circulation models, *J. Geophys. Res.*, *110*, A10306, doi:10.1029/2005JA011160.
- Solomon, S. C., S. M. Bailey, and T. N. Woods (2001), Effect of solar soft X-rays on the lower atmosphere, *Geophys. Res. Lett.*, *28*, 2149, doi:10.1029/2001GL012866.
- Thayer, J. P., J. Lei, J. M. Forbes, E. K. Sutton, and R. S. Nerem (2008), Thermospheric density oscillations due to periodic solar wind high-speed streams, *J. Geophys. Res.*, *113*, A06307, doi:10.1029/2008JA013190.
- Tobiska, W. K., S. D. Bouwer, and B. R. Bowman (2008), The development of new solar indices for use in thermospheric density modeling, *J. Atmos. Space Phys.*, *70*, 803, doi:10.1016/j.jastp.2007.11.001.
- Warren, H. P. (2006), NRLEUV 2: A new model of solar EUV irradiance variability, *Adv. Space Res.*, *37*, 359, doi:10.1016/j.asr.2005.10.028.
- Woods, T., F. Eparvier, S. Bailey, S. C. Solomon, G. Rottman, G. Lawrence, R. Roble, O. R. White, J. Lean, and W. K. Tobiska (1998), TIMED solar EUV experiment, *Proc. SPIE*, *3442*, 180, doi:10.1117/12.330255.
- Woods, T. N., S. M. Bailey, W. K. Peterson, S. C. Solomon, H. P. Warren, F. G. Eparvier, H. Garcia, C. W. Carlson, and J. P. McFadden (2003), Solar extreme ultraviolet variability of the X-class flare on April 21, 2002 and the terrestrial photoelectron response, *Space Weather*, *1*(1), 1001, doi:10.1029/2003SW000010.
- Woods, T. N., et al. (2010), Extreme Ultraviolet Variability Experiment (EVE) on the Solar Dynamics Observatory (SDO): Overview of science objectives, instrument design, data products, and model developments, *Sol. Phys.*, *275*, 115, doi:10.1007/s11207-009-9487-6.